

Chapter 8

Microwave-Driven Dynamics of Magnetic Skyrmions Under a Tilted Magnetic Field: Magnetic Resonances, Translational Motions, and Spin-Motive Forces



Masahito Mochizuki

Abstract Magnetic skyrmions, particle-like magnetic textures characterized by a quantized topological invariant in magnets with broken spatial inversion symmetry, are currently attracting enormous research interest in the field of spintronics. Recent intensive studies have uncovered that magnetic skyrmions exhibit rich physical phenomena and device functions originating from their topological nature. In this chapter, we discuss microwave-induced dynamical phenomena of magnetic skyrmions associated with their peculiar spin-wave modes. In particular, we focus on a situation that the magnetic skyrmions are confined in a quasi-two-dimensional thin-plate magnet under application of a static magnetic field tilted from the perpendicular direction. It is theoretically demonstrated that the spin-wave excitations of these magnetic skyrmions by microwave irradiation give rise to translational motion of the skyrmions and generation of the DC electric voltages. These phenomena indicate that rich physics and functionalities are hidden in the microwave-driven skyrmion dynamics under a tilted magnetic field.

8.1 Introduction

Magnetic skyrmions, topological magnetic entities carrying a quantized topological invariant in magnets without spatial inversion symmetry, are currently attracting a great deal of research interest [1–7]. In the early 1960s, an English theoretical physicist, Tony Hilton Royle Skyrme, proposed a theoretical concept of Skyrmion as a soliton solution of the nonlinear sigma model to account for the stability of hadron in the nuclear physics [8, 9]. This originally proposed skyrmion is a hedgehog-like particle composed of field vectors pointing in every direction wrapping a sphere

M. Mochizuki (✉)

Department of Applied Physics, Waseda University, 3-4-1 Okubo, Shinjuku-ku,

Tokyo 169-8555, Japan

e-mail: masa_mochizuki@waseda.jp

© Springer Nature Switzerland AG 2021

E. Kamenetskii (ed.), *Chirality, Magnetism and Magnetolectricity*,

Topics in Applied Physics 138,

https://doi.org/10.1007/978-3-030-62844-4_8

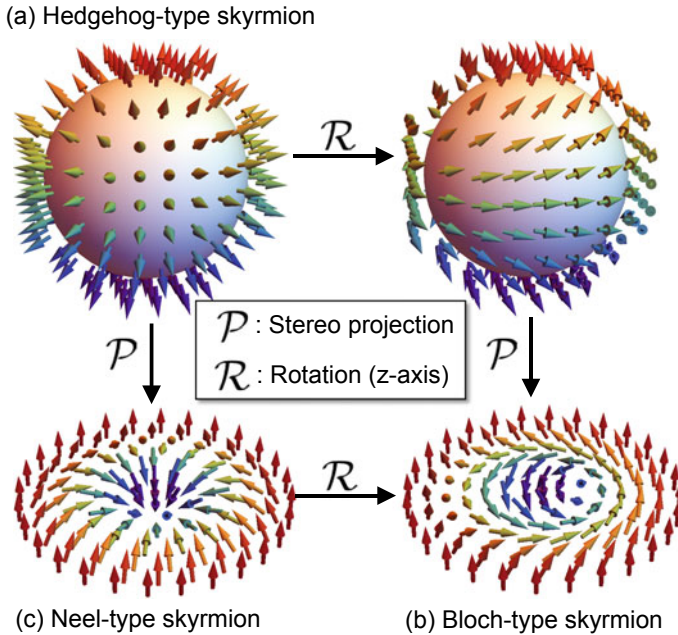


Fig. 8.1 **a** Hedgehog-type skyrmion originally proposed by Tony Skyrme in early 1960s. **b** Bloch-type skyrmion with magnetizations rotating within a plane normal to the radial direction. **c** Neel-type skyrmion with magnetizations rotating within a plane parallel to the radial direction. These three types of skyrmions are mutually related via a stereo projection and a rotation with respect to the z axis

(Fig. 8.1a). About 30 years later, Bogdanov and his coworkers theoretically predicted realization of these conceptual objects in magnets as textures of magnetizations [10, 11]. They proposed that the magnetic skyrmions can emerge in magnets with spatial inversion asymmetry as vortex-like (Fig. 8.1b) or fountain-like (Fig. 8.1c) magnetic textures. These magnetic textures can be reproduced by a stereo projection of the original hedgehog-type skyrmion onto a two-dimensional plane. This theoretical prediction was indeed confirmed by experimental discoveries of magnetic skyrmions in B20-type alloys [12–14]. In 2009, a small-angle neutron scattering experiment reported a discovery of skyrmion crystals in which numerous magnetic skyrmions are crystallized into a hexagonal form in a chiral-lattice magnet MnSi [12]. In 2010, a Lorentz transmission electron microscopy reported an observation of real-space images of skyrmion crystals in $\text{Fe}_{1-x}\text{Co}_x\text{Si}$ [13]. This experiment also revealed that magnetic skyrmions emerge not only as the crystallized form but also as isolated defects in the ferromagnetic phase. Subsequently, the magnetic skyrmions have been discovered in various magnetic systems such as other chiral-lattice magnets (FeGe [14], Cu_2OSeO_3 [15], and βMn -type Co-Mn-Zn alloys [16]), polar magnets (GaV_4S_8 [17], GaV_4Se_8 [18, 19], $\text{Mn}_{1.4}\text{Pt}_{0.9}\text{Pd}_{0.1}\text{Sn}$ [20], VOSe_2O_5 [21]), and magnetic heterostructures [3, 22–24].

All the above-mentioned magnets and magnetic systems have structures with broken spatial inversion symmetry. Consequently, the Dzyaloshinskii-Moriya interaction becomes active, which favors rotating alignment of magnetizations with a pitch angle of 90° [25, 26]. This interaction strongly competes with the ferromagnetic exchange interaction, which favors parallel alignment of magnetizations. The keen competition between these two interactions results in the formation of helical magnetic order with a moderate pitch angle. When an external magnetic field is applied to this helical magnetic state, a skyrmion crystal appears on a plane normal to the applied magnetic field. In each skyrmion constituting the skyrmion crystal, the magnetizations at periphery are oriented along the external magnetic field so as to maximize an energy gain of the Zeeman interaction. The magnetizations gradually rotate when we move from the periphery to the center along the radial direction. Eventually, the magnetizations are oriented antiparallel to the external magnetic field at the center. In bulk magnets, these two-dimensional skyrmions are stacked along the three-dimensional direction to form tubular structures. It should also be mentioned that the magnetic skyrmions can be classified into several types according to the way of the magnetization rotation. Skyrmions in which the magnetizations rotate within planes perpendicular (parallel) to the radial direction are called Bloch type (Neel type). The three types of skyrmions, i.e., the hedgehog-type, the Bloch-type, and the Neel-type, are mutually related via the rotational operation with respect to the z axis and the stereo projection (see Fig. 8.1).

Skyrmions are characterized by a quantized topological invariant, which represents a sum of the solid angles spanned by three neighboring normalized magnetization vectors $\mathbf{m}(\mathbf{r})$,

$$\int_{\text{UC}} dx dy \left(\frac{\partial \mathbf{m}}{\partial x} \times \frac{\partial \mathbf{m}}{\partial y} \right) \cdot \mathbf{m} = 4\pi Q \quad (Q = \pm 1). \quad (8.1)$$

Here the integration is taken over the area of the unit cell (UC). Because the magnetization vectors constituting a skyrmion point in every direction wrapping a sphere, the sum of the solid angles is identical to the surface area of a unit sphere ($\mp 4\pi$). Consequently, the quantity Q , which is called the topological charge or the skyrmion number, becomes $+1$ or -1 . The sign is positive (negative) when the magnetization at the core points upward (downward). This number does not change upon continuous variation of the magnetization alignment. Because the value of Q is zero for ferromagnetic and spiral magnetic orders, magnetic skyrmions belong to a different topological class from these magnetic structures. This means that magnetic skyrmions cannot be created or erased in a uniform ferromagnetic state by continuous variation of the magnetization alignment. Instead, a local flop of the magnetization is needed to create and erase them, which necessarily requires a large cost of energy, magnitude of which is comparable to the energy scale of the ferromagnetic exchange interaction. The topological protection by this large energy barrier makes magnetic skyrmions robust against external assitations and perturbations.

This significant stability is one of the advantageous properties of magnetic skyrmions for spintronics application to ubiquitous magnetic devices in the coming

IoT era. Future electronic devices sustaining the IoT society such as sensor, logic, and storage devices are demanded to keep working normally with a little energy supply in harsh environments such as weather-beaten places, extremely hot or cold areas, places suffered from continuous mechanical shocks and vibrations, and outer spaces exposed by cosmic rays. Therefore, the devices should have the resistance against thermal fluctuations, the durability against radioactive rays, and the sustainability with conserved electric power. From this viewpoint, the magnetic skyrmions have high potentials as building blocks of the next-generation magnetic devices because they have not only the topologically protected stability but also the nanoscale ultrasmall size and the operability with ultralow energy consumption.

Aiming at the technical applications, magnetic skyrmions have attracted a great deal of interest recently as a target of the spintronics research, and several intriguing phenomena and useful device functions have been discovered or proposed successively. In particular, the dynamical magnetoelectric phenomena and the microwave device functions associated with their peculiar microwave-active spin-wave modes [27] are important examples [6, 7]. In this chapter, we discuss recent theoretical studies on the microwave-induced physical phenomena and device functions of magnetic skyrmions by particularly focusing on theoretical proposals of the microwave-driven translational motion [28–30] and the efficient conversion of microwaves to DC electric voltages [31] expected in the spin-wave excitations of magnetic skyrmions in a quasi-two-dimensional magnet under a tilted external magnetic field.

8.2 Spin Model of the Skyrmion-Hosting Magnets

In this chapter, we deal with magnetic skyrmions confined in a quasi-two-dimensional thin-plate magnet with broken spatial inversion symmetry. The simplest spin model for such quasi-two-dimensional skyrmion-hosting magnets is given in a continuum form as [32],

$$\mathcal{H}_0 = \int dr \left[\frac{J}{2a} (\nabla \mathbf{m})^2 + \frac{D}{a^2} \mathbf{m} \cdot (\nabla \times \mathbf{m}) - \frac{1}{a^3} \mathbf{H} \cdot \mathbf{m} \right] \quad (8.2)$$

By dividing the continuum space into cubic cells, the above continuum model is reduced to a classical Heisenberg model on a square lattice as [33],

$$\mathcal{H}_0 = -J \sum_{i,\mu} \mathbf{m}_i \cdot \mathbf{m}_{i+\hat{\mu}} - \sum_{i,\mu} \mathbf{D}_\mu \cdot (\mathbf{m}_i \times \mathbf{m}_{i+\hat{\mu}}) - \mathbf{H}_{\text{ex}} \cdot \sum_i \mathbf{m}_i. \quad (8.3)$$

Here \mathbf{m}_i represents a normalized magnetization vector on the i th lattice site. The first term represents the ferromagnetic exchange interaction, whereas the second term represents the Dzyaloshinskii-Moriya interaction. The third term depicts the Zeeman coupling associated with an external magnetic field \mathbf{H}_{ex} . Types of the skyrmions are determined by the structure of the Moriya vectors \mathbf{D}_μ ($\mu = x, y$). The Bloch-type

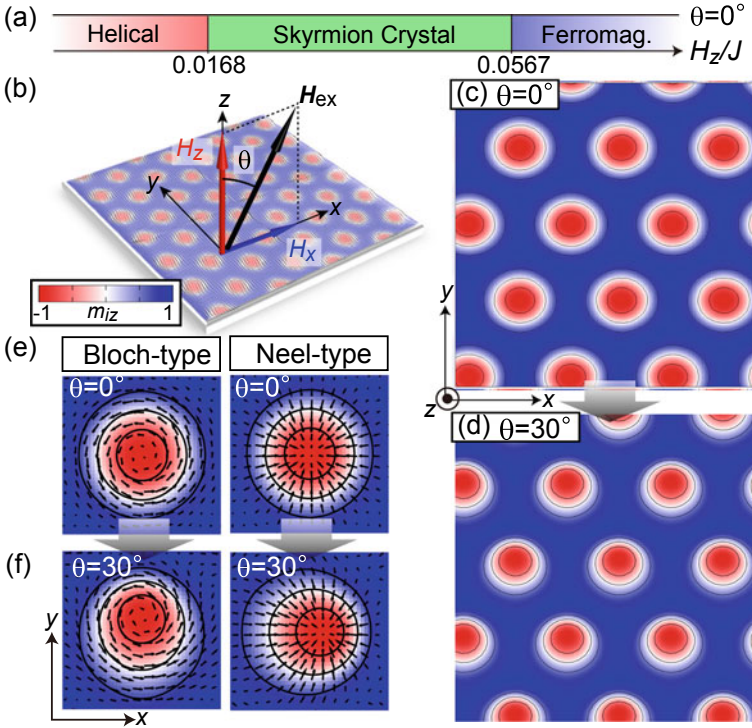


Fig. 8.2 **a** Theoretical phase diagram of the spin model in (8.3) on a square lattice as a function of the magnetic-field strength H_z when $\mathbf{H}_{\text{ex}} = (0, 0, H_z)$ is applied normal to the plane. Here the strength of the DM interaction is set to be $D/J = 0.27$. **b** Thin-plate specimen of chiral-lattice magnet hosting a skyrmion crystal under a magnetic field $\mathbf{H}_{\text{ex}} = (H_z \tan \theta, 0, H_z)$ with a tilting angle of θ . **c, d** Skyrmion crystal under a perpendicular [tilted] \mathbf{H}_{ex} field with $\theta = 0^\circ$ [$\theta = 30^\circ$]. **e, f** Magnetization configurations of Bloch-type and the Neel-type skyrmions under a perpendicular [tilted] \mathbf{H}_{ex} field (Reproduced from [29].)

skyrmions are produced by $\mathbf{D}_x = (D, 0, 0)$ and $\mathbf{D}_y = (0, D, 0)$, whereas the Neel-type skyrmions are produced by $\mathbf{D}_x = (0, D, 0)$ and $\mathbf{D}_y = (-D, 0, 0)$. Figure 8.2a shows a theoretical phase diagram of this spin model for $D/J = 0.27$ at $T = 0$ as a function of the magnetic-field strength H_z when $\mathbf{H}_{\text{ex}} = (0, 0, H_z)$ is applied perpendicular to the two-dimensional plane. This phase diagram exhibits the skyrmion-crystal phase in a region of moderate field strength sandwiched by the helical phase and the field-polarized ferromagnetic phase.

The lattice spacing of skyrmion crystal, i.e., the distance between cores of neighboring skyrmions in the skyrmion crystal is determined by competition between the Dzyaloshinskii-Moriya interaction and the ferromagnetic exchange interaction, which favor rotating and parallel magnetization alignments, respectively. A stronger Dzyaloshinskii-Moriya interaction causes more rapid rotation of the magnetizations, which results in a smaller skyrmion size. Because $\phi \sim D/(\sqrt{2}J)$ holds for the

Table 8.1 Unit conversion table when $J = 1$ meV

	Dimensionless quantity	Corresponding value with units
Exchange int.	$J = 1$	$J = 1$ meV
Magnetic field	$H = 1$	$J/g\mu_B = 8.64$ T
Time	$t = 1$	$\hbar/J = 0.66$ ps
Frequency $f = \omega/2\pi$	$\omega = 1$	$J/h = 241$ GHz

magnetization rotation angle ϕ , the spatial period in the skyrmion crystal becomes $\lambda_m \sim 2\pi a/\phi$ when $\mathbf{H}_{\text{ex}} = 0$ where a is the lattice constant. Even when \mathbf{H}_{ex} is finite, this spatial period does not change so much although the magnetization rotation is no longer uniform. Therefore, the ratio $D/J = 0.27$ gives $\lambda_m \sim 18$ nm if we assume a typical lattice constant of $a = 0.5$ nm, which corresponds to the experimentally observed skyrmion size in MnSi [12, 34]. When $J = 1$ meV is the energy units, the dimensionless field strength $H_z = 1$ corresponds to ~ 8.64 T. Therefore, the threshold magnetic fields of $H_{c1} = 0.0168$ and $H_{c2} = 0.0567$ in the theoretical phase diagram of Fig. 8.2a correspond to 0.145 T and 0.49 T, respectively. These values again coincide well with the experimentally observed threshold magnetic fields of ~ 0.15 T and ~ 0.45 T for MnSi at low temperatures [34]. The unit conversions when $J = 1$ meV are summarized in Table 8.1.

We examine the cases in which the \mathbf{H}_{ex} field is tilted from the normal direction ($\parallel z$) of the quasi-two-dimensional system towards the x direction. The magnetic field is given in the form,

$$\mathbf{H}_{\text{ex}} = (H_x, 0, H_z), \quad (8.4)$$

with $H_x = H_z \tan \theta$, where the angle θ describes to what extent the \mathbf{H}_{ex} field is tilted towards the x direction (Fig. 8.2b). In bulk materials, the magnetic skyrmions usually appear on a plane normal to the \mathbf{H}_{ex} field and have a circularly symmetric shape. This circular symmetry is kept even when a direction of the \mathbf{H}_{ex} field is changed because the stacked magnetic skyrmions can change their tubular orientations to keep the skyrmion plane normal to the \mathbf{H}_{ex} field in the three-dimensional systems so as to maximize the energy gain of the Zeeman interaction. On the other hand, when the skyrmions are confined in a system of strong two-dimensionality, the situation is no longer the same. Although the skyrmions have a circularly symmetric shape when the \mathbf{H}_{ex} field applied perpendicular to the two-dimensional plane (Fig. 8.2c, e), they become to have a disproportionate weight in the magnetization distribution and lose their circular symmetry when the \mathbf{H}_{ex} field is tilted (Fig. 8.2d, f). In fact, these deformed skyrmions under a tilted \mathbf{H}_{ex} field turn out to exhibit intriguing microwave-related physical phenomena and device functions.

The microwave-induced dynamics of magnetic skyrmions are investigated by the micromagnetic simulations based on the Landau–Lifshitz–Gilbert equation. The equation is given by,

$$\frac{d\mathbf{m}_i}{dt} = -\gamma \mathbf{m}_i \times \mathbf{H}_i^{\text{eff}} + \frac{\alpha_G}{m} \mathbf{m}_i \times \frac{d\mathbf{m}_i}{dt}. \quad (8.5)$$

The first term of the right-hand side is the gyrotropic term where $\gamma = g\mu_B/\hbar$ is the gyromagnetic ratio. This term describes the precessional motion of magnetizations \mathbf{m}_i around the effective local magnetic field $\mathbf{H}_i^{\text{eff}}$. The second term is the Gilbert-damping term introduced phenomenologically to depicts the dissipation of gyration energy. The effective magnetic field $\mathbf{H}_i^{\text{eff}}$, which acts on the local magnetization \mathbf{m}_i , is calculated from the Hamiltonian $\mathcal{H} = \mathcal{H}_0 + \mathcal{H}'(t)$ as,

$$\mathbf{H}_i^{\text{eff}} = -\frac{1}{\gamma\hbar} \frac{\partial \mathcal{H}}{\partial \mathbf{m}_i}, \quad (8.6)$$

where \mathcal{H}_0 is the model Hamiltonian given by (8.3). Here an additional term of the Hamiltonian $\mathcal{H}'(t)$ is introduced, which describes the dynamical coupling between the skyrmion magnetizations and a time-dependent magnetic field or a microwave magnetic field in the form,

$$\mathcal{H}'(t) = -\mathbf{H}(t) \cdot \sum_i \mathbf{m}_i. \quad (8.7)$$

The initial magnetic configuration of a skyrmion crystal is prepared by the Monte-Carlo thermalization at low temperatures and by further relaxing it in the micromagnetic simulation without applying a microwave magnetic field. The microwave-induced dynamics are simulated by applying a microwave field to thus obtained sufficiently converged skyrmion-crystal configuration.

8.3 Microwave-Active Spin-Wave Modes

A skyrmion crystal confined in a quasi-two-dimensional magnet exhibits characteristic microwave-active spin-wave modes (Fig. 8.3a–c) [27]. An in-plane polarized microwave magnetic field $\mathbf{H}^\omega \parallel \mathbf{x}, \mathbf{y}$ activates a pair of rotation modes, in which all the skyrmions constituting the skyrmion crystal uniformly circulate in counterclockwise and clockwise ways. The counterclockwise rotation mode has a lower resonance frequency and a larger intensity than the clockwise rotation mode. On the other hand, an out-of-plane polarized microwave magnetic field $\mathbf{H}^\omega \parallel \mathbf{z}$ activates the breathing mode in which all the skyrmions in the skyrmion crystal uniformly expand and shrink in an oscillatory manner. Then how are these spin-wave modes modulated when the \mathbf{H}_{ex} field is tilted from the perpendicular direction?

The spin-wave modes and their resonance frequencies can be identified by calculating the dynamical magnetic susceptibility,

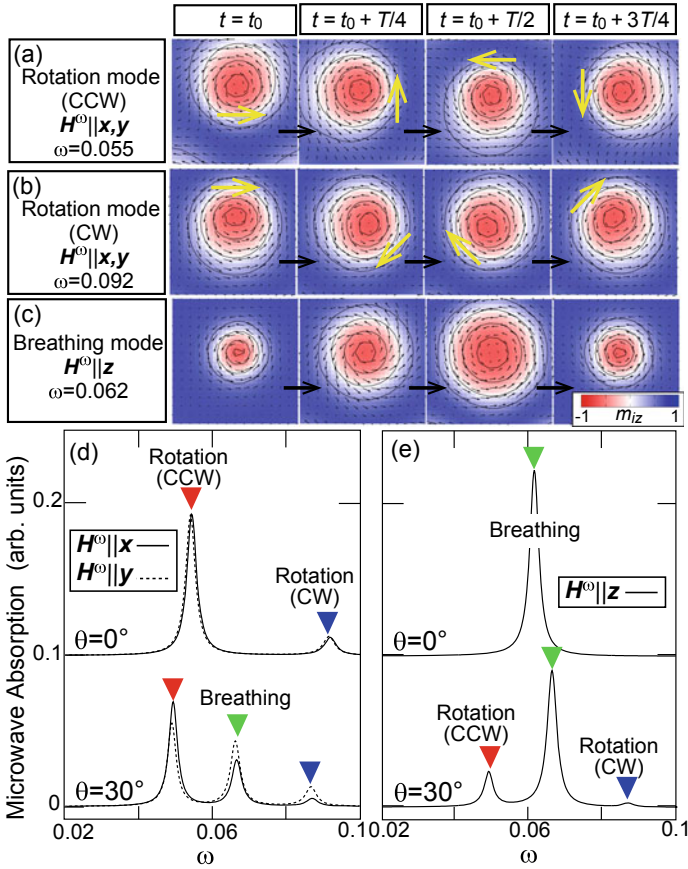


Fig. 8.3 a–c Simulated snapshots of the three spin-wave modes of a skyrmion crystal confined in a quasi-two-dimensional thin-plate magnet under a perpendicular H_{ex} field. Here one skyrmion in the skyrmion crystal is focused on because all the skyrmions oscillate uniformly in each mode. The two rotation modes with counterclockwise (CCW) and clockwise (CW) rotation senses are active to an in-plane microwave magnetic field $H^\omega \parallel x, y$, whereas the breathing mode is active to an out-of-plane microwave magnetic field $H^\omega \parallel z$. **d** Calculated microwave absorption spectra under perpendicular ($\theta = 0^\circ$) and tilted ($\theta = 30^\circ$) H_{ex} fields as functions of the microwave angular frequency ω for the in-plane microwave field $H^\omega \parallel x, y$. **e** Those for the out-of-plane microwave field $H^\omega \parallel z$. Here the simulations are performed for $J = 1$, $D/J = 0.27$, $H_z = 0.036$, $H^\omega = 0.0018$, and $\alpha_G = 0.02$ (Reproduced from [29].)

$$\chi_\mu(\omega) = \frac{\Delta M_\mu(\omega)}{\mu_0 H_\mu(\omega)} \quad (\mu = x, y, z), \quad (8.8)$$

where $H_\mu(\omega)$ and $\Delta M_\mu(\omega)$ are the Fourier transforms of the time-dependent magnetic field $\mathbf{H}(t)$ and the simulated time-profile of the net magnetization $\Delta \mathbf{M}(t) = \mathbf{M}(t) - \mathbf{M}(0)$ with $\mathbf{M}(t) = \frac{1}{N} \sum_{i=1}^N \mathbf{m}_i(t)$. In the calculations, a short rectangular pulse is used for $\mathbf{H}(t)$ whose component is given by,

$$H_\mu(t) = \begin{cases} H_{\text{pulse}} & 0 \leq t \leq 1 \\ 0 & \text{others} \end{cases} \quad (8.9)$$

where $t = (J/\hbar)\tau$ is the dimensionless time with τ being the real time. An advantage of using the short pulse is that the Fourier component $H_\mu(\omega)$ becomes constant being independent of ω up to first order in $\omega\Delta t$ for a sufficiently short duration Δt with $\omega\Delta t \ll 1$. The Fourier component is

$$H_\mu(\omega) = \int_0^{\Delta t} H_{\text{pulse}} e^{i\omega t} dt = \frac{H_{\text{pulse}}}{i\omega} (e^{i\omega\Delta t} - 1) \sim H_{\text{pulse}}\Delta t. \quad (8.10)$$

Consequently, we obtain the relationship $\chi_\mu(\omega) \propto \Delta M_\mu(\omega)$. The imaginary part of thus calculated $\chi_\mu(\omega)$ corresponds to the microwave absorption spectrum. Figure 8.3d shows the spectra for the in-plane polarized microwave field $\mathbf{H}^\omega \parallel \mathbf{x}, \mathbf{y}$ under perpendicular ($\theta = 0^\circ$) and tilted ($\theta = 30^\circ$) \mathbf{H}_{ext} fields, whereas Fig. 8.3e shows the spectra for the out-of-plane polarized microwave field $\mathbf{H}^\omega \parallel \mathbf{z}$ [29]. When the \mathbf{H}_{ext} field is perpendicular ($\theta = 0^\circ$), two spectral peaks appear in Fig. 8.3d originating from the two rotation modes, whereas a single peak appears in Fig. 8.3e originating from the breathing mode, indicating that the in-plane (out-of-plane) microwave field can activate the rotation modes (the breathing mode) only when the \mathbf{H}_{ext} field is perpendicular. On the other hand, when the \mathbf{H}_{ext} field is tilted ($\theta = 30^\circ$), three spectral peaks appear in both Fig. 8.3d, e, indicating that all the three spin-wave modes become active to both microwave polarization under the tilted \mathbf{H}_{ext} field.

8.4 Microwave-Magnetic-Field-Driven Translational Motion of Skyrmion Crystal

The continuous spin-wave excitation by microwave irradiation under a tilted \mathbf{H}_{ext} field can induce translational motion of a skyrmion crystal [28, 29]. Figure 8.4 shows simulated snapshots of a skyrmion crystal driven by an in-plane microwave field $\mathbf{H}^\omega \parallel \mathbf{x}$ (right upper panel) and the same skyrmion crystal driven by an out-of-plane microwave field $\mathbf{H}^\omega \parallel \mathbf{z}$ (right lower panel) at $t = 400$ ns after the microwave irradiation commences. The figure also shows the initial configuration of the skyrmion crystal at $t = 0$ (left panel) under application of the tilted magnetic field $\mathbf{H}_{\text{ex}} =$

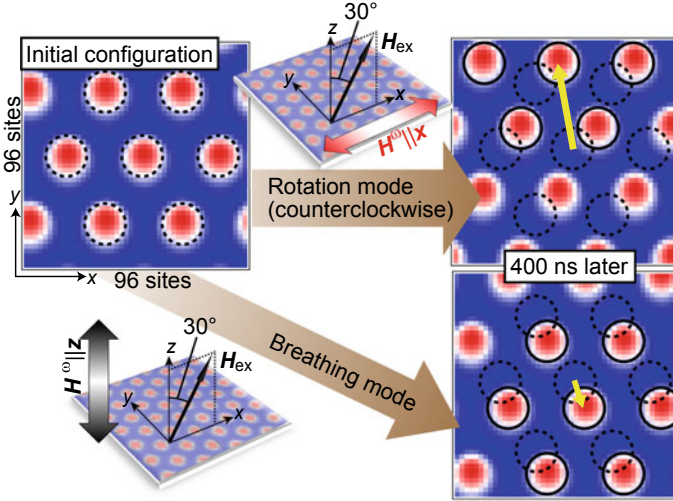


Fig. 8.4 Microwave-driven translational motion of a skyrmion crystal in a quasi-two-dimensional system under a tilted \mathbf{H}_{ext} field with $\theta = 30^\circ$. The system is irradiated by a microwave field $H_\mu^\omega \sin \omega t$ ($\mu = x, y, z$) with $H_\mu^\omega = 0.0006$. The skyrmion crystal moves approximately towards the positive (negative) y direction when a microwave field $\mathbf{H}^\omega \parallel \mathbf{x}$ ($\mathbf{H}^\omega \parallel \mathbf{z}$) with $\omega = 0.0494$ ($\omega = 0.0666$) activates the counterclockwise rotation (breathing) mode. Displacement vectors connecting the original position (dashed circles) and the position after 400-ns duration (solid circles) are indicated by the thick arrows in the right panels. The simulations are performed for $J = 1$, $D/J = 0.27$, $H_z = 0.036$, and $\alpha_G = 0.04$ (Reproduced from [29].)

$(H_z \tan \theta, 0, H_z)$ with $H_z = 0.036$ and $\theta = 30^\circ$. Here, the microwave field is given by $H_\mu^\omega \sin \omega t$ ($\mu = x, y, z$) with $H_\mu^\omega = 0.0006$. The displacement vectors connecting the original position and the position at $t = 400$ ns are indicated by thick arrows shown in the right-side panels. When the microwave field $\mathbf{H}^\omega \parallel \mathbf{x}$ with $\omega = 0.0494$ activates the counterclockwise rotation mode, the skyrmion crystal propagates in a direction close to the positive y direction, whereas the same skyrmion crystal propagates in a direction close to the negative y direction when $\mathbf{H}^\omega \parallel \mathbf{z}$ with $\omega = 0.0666$ activates the breathing mode. It is also found that the travel distance in the former case is much longer than that in the latter case, which indicates that the in-plane microwave field $\mathbf{H}^\omega \parallel \mathbf{x}$ drives much faster motion of the skyrmion crystal than the out-of-plane microwave field $\mathbf{H}^\omega \parallel \mathbf{z}$.

Figure 8.5a, b display the simulated microwave frequency dependence of the drift velocity $\mathbf{v} = (v_x, v_y)$ of the driven skyrmion crystal under a tilted \mathbf{H}_{ext} field for different microwave polarizations. Apparently, the velocities are enhanced to have peaks at the resonance frequencies that correspond to the spin-wave modes, indicating that the resonant spin-wave excitations of skyrmion crystal indeed drive its quick translational motion. The velocity is highest with $v_x \sim 0.04$ m/s when the in-plane

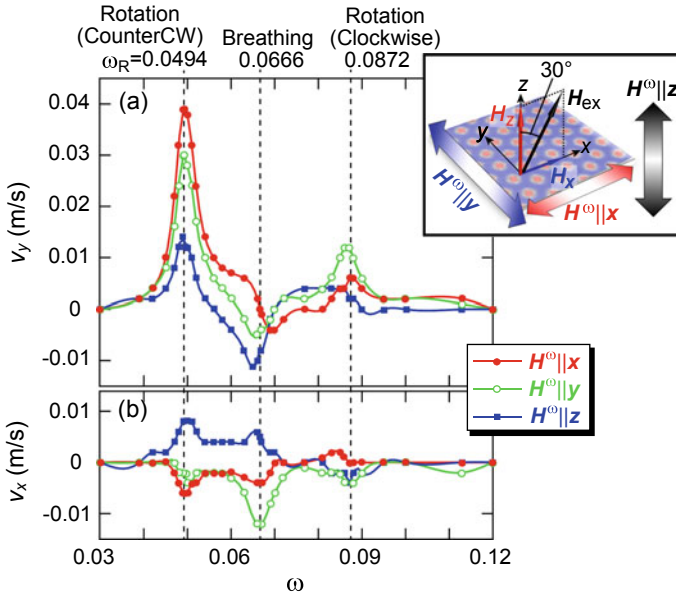


Fig. 8.5 Calculated microwave frequency dependence of the velocity $\mathbf{v} = (v_x, v_y)$ for translational motion of the skyrmion crystal induced by a microwave field \mathbf{H}^ω under a tilted \mathbf{H}_{ext} field $\mathbf{H}_{\text{ex}} = (H_z \tan \theta, 0, H_z)$ with $H_z = 0.036$ and $\theta = 30^\circ$. The system is irradiated by a microwave field $H_\mu^\omega \sin \omega t$ ($\mu = x, y, z$) with $H_\alpha^\omega = 0.0006$ where $\omega = 2\pi f$ is its angular frequency. The velocities show peaks at the resonant frequencies of the spin-wave modes, while their signs vary depending on the mode and the microwave polarization (Reproduced from [29]).

microwave field $\mathbf{H}^\omega \parallel \mathbf{x}$ activates the counterclockwise rotation mode. It is also found that the speed and the direction of this translational motion sensitively depend on the excited spin-wave mode and the microwave polarization.

8.5 Microwave-Electric-Field-Driven Translational Motion of Isolated Skyrmions

In this section, we discuss an efficient method to drive isolated magnetic skyrmions embedded in ferromagnetic environment with microwave *electric* fields instead of microwave *magnetic* fields [30]. As mentioned in the introduction section, the magnetic skyrmions appear not only as a crystallized form but also as isolated defects in the ferromagnetic phase. Recently possible application of magnetic skyrmions to high-performance memory devices are studied intensively. For the usage as information carriers in memory devices, isolated magnetic skyrmions rather than crystallized ones are recognized to be convenient. However, when a microwave magnetic field is applied to a device to activate the isolated skyrmion defects, it is unavoidable to

excite a vast majority of background ferromagnetic magnetizations, which hinders the resonance modes of the skyrmion defects.

To solve this problem, it was recently proposed theoretically that isolated magnetic skyrmions can be selectively activated using microwave electric fields without exciting ferromagnetic resonances, in contrast to conventional methods using microwave magnetic fields. It was also demonstrated by numerical simulations that the selective activation of a skyrmion can efficiently drive its translational motion in a ferromagnetic nanotrack under application of a tilted \mathbf{H}_{ext} field.

We consider a magnetic bilayer system with a ferromagnetic layer fabricated on top of a heavy-metal layer with strong spin-orbit interaction, where the Dzyaloshinskii-Moriya interaction becomes active at their interface due to the spatial inversion asymmetry to form Neel-type skyrmions. A tilted magnetic field $\mathbf{H}_{\text{ex}} = (H_x, 0, H_z)$ with $H_x = H_z \tan \theta$ is applied to this bilayer system. To investigate microwave-driven phenomena of skyrmions in this system, the following classical Heisenberg model on a square lattice was employed,

$$\begin{aligned} \mathcal{H} = & -J \sum_{\langle i,j \rangle} \mathbf{m}_i \cdot \mathbf{m}_j - [\mathbf{H}_{\text{ex}} + \mathbf{H}(t)] \cdot \sum_i \mathbf{m}_i \\ & + D(t) \sum_i [(\mathbf{m}_i \times \mathbf{m}_{i+\hat{x}}) \cdot \hat{y} - (\mathbf{m}_i \times \mathbf{m}_{i+\hat{y}}) \cdot \hat{x}], \end{aligned} \quad (8.11)$$

where \mathbf{m}_i is the normalized magnetization vector. In this Hamiltonian, a time-dependent magnetic field or a microwave magnetic field $\mathbf{H}(t) = (0, 0, H_z(t))$ with $H_z(t) = H_z^\omega \sin(\omega t)$ is taken into account via the Zeeman coupling term. On the other hand, a time-dependent electric field $\mathbf{E}(t) = (0, 0, E_z(t))$ with $E_z(t) = E_z^\omega \sin(\omega t)$ applied perpendicular to the sample plane is incorporated via the time-dependent interfacial Dzyaloshinskii-Moriya interaction. The strength of this interaction can be tuned by applying a gate electric field normal to the plane via varying the extent of the spatial inversion asymmetry [35–37]. Importantly, the coefficient $D(t) = D_0 + \Delta D(t)$ has two components, specifically, a steady component D_0 and a $\mathbf{E}(t)$ -dependent component $\Delta D(t) = \kappa E_z(t)$ with κ being the coupling constant.

A time profile of the net magnetization $M_z(t) = (1/N) \sum_i m_{zi}(t)$ and $\Delta M_z(t) = M_z(t) - M_z(0)$ are simulated by numerically solving the Landau–Lifshitz–Gilbert equation after application of a short pulse $H_z(t)$ or $E_z(t)$ with duration of $\Delta t = 1$. From its Fourier transform ΔM_z^ω , the dynamical magnetic and electromagnetic susceptibilities χ^{mm} and χ^{em} are calculated as,

$$\chi^{\text{mm}}(\omega) = \frac{\Delta M_z^\omega}{\mu_0 H_{\text{pulse}}}, \quad \chi^{\text{em}}(\omega) = \sqrt{\frac{\mu_0}{\epsilon_0}} \frac{\Delta M_z^\omega}{E_{\text{pulse}}} \quad (8.12)$$

Note that the magnetic susceptibility χ^{mm} represents the response of the magnetizations to the microwave magnetic field $\mathbf{H}(t)$, whereas the electromagnetic susceptibility χ^{em} represents the response of the magnetizations to the microwave electric field $\mathbf{E}(t)$.

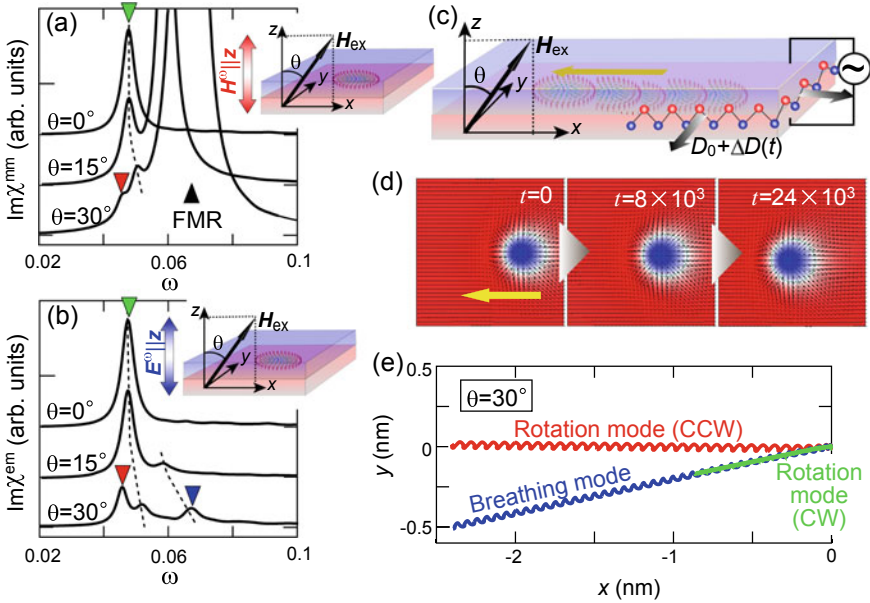


Fig. 8.6 **a, b** Microwave absorption spectra $\text{Im}\chi^{\text{mm}}(\omega)$ [$\text{Im}\chi^{\text{em}}(\omega)$] when a quasi-two-dimensional ferromagnet with a skyrmion defect under perpendicular ($\theta = 0^\circ$) and tilted ($\theta \neq 0^\circ$) \mathbf{H}_{ext} field is irradiated with an out-of-plane polarized microwave magnetic [electric] field $\mathbf{H}^\omega \parallel \mathbf{z}$ [$\mathbf{E}^\omega \parallel \mathbf{z}$]. The spectra $\text{Im}\chi^{\text{mm}}(\omega)$ for various angles θ indicate that the ferromagnetic resonance mode becomes active to the microwave magnetic field $\mathbf{H}^\omega \parallel \mathbf{z}$ when the \mathbf{H}_{ext} field is tilted, and its intensity becomes rapidly enhanced as θ increases, although it is silent when the \mathbf{H}_{ext} field is perpendicular. In contrast, the spectra $\text{Im}\chi^{\text{em}}(\omega)$ indicate that the microwave electric field $\mathbf{E}^\omega \parallel \mathbf{z}$ can selectively activate resonance modes of the skyrmion defect without exciting the background ferromagnetic magnetizations. **c** Schematic illustration of an experiment for the temporal variation of the interfacial Dzyaloshinskii-Moriya interaction by application of a microwave electric field to the magnetic bilayer system under a tilted \mathbf{H}_{ext} field. **d** Simulated snapshots of the translational motion of the driven skyrmion defect. **e** Trajectories of a driven skyrmion defect for three different spin modes activated by the microwave electric field. The simulations for **d** and **e** are performed for $J = 1$, $D_0/J = 0.27$, $\kappa E_z^\omega = 0.05D_0$, $H_z = 0.057$, $\theta = 30^\circ$, and $\alpha_G = 0.04$ (Reproduced from [30].)

Figure 8.6a displays imaginary parts of the calculated dynamical magnetic susceptibilities $\text{Im}\chi^{\text{mm}}$ of a ferromagnetic system with a single skyrmion defect under application of the out-of-plane microwave magnetic field ($\mathbf{H}^\omega \parallel \mathbf{z}$) for various values θ . The calculations are performed for a ferromagnetic system of 160×160 sites with periodic boundary conditions, in which one skyrmion exists as a defect. When $\theta = 0^\circ$, only a single peak appears in the spectrum indicating that only the breathing mode of the skyrmion defect is activated without exciting the background ferromagnetic magnetizations. However, as θ increases, the intensity of the breathing mode decreases, and, alternatively, a large spectral peak due to the ferromagnetic resonance mode appears in the higher frequency regime. Namely, under the tilted \mathbf{H}_{ext} field,

the microwave magnetic field cannot avoid activating the intense ferromagnetic resonance mode, which inevitably results in large loss of energy and significant rise of temperature.

To drive isolated skyrmions in the ferromagnetic phase efficiently, it is necessary to activate the skyrmions selectively avoiding the situation that the weak skyrmion resonance modes are masked by the intense ferromagnetic resonance mode. This seemingly impossible operation can be achieved by taking advantage of the microwave electric field. More concretely, when a microwave electric field is applied to a magnetic bilayer system or a thin-film specimen of chiral-lattice magnet fabricated on insulating substrate, the isolated skyrmions can be selectively activated through temporal variation of the extent of spatial inversion asymmetry and resulting temporal oscillation of the Dzyaloshinskii-Moriya interaction. The calculated microwave absorption spectra (the imaginary parts of the electromagnetic susceptibilities $\text{Im}\chi^{\text{em}}$) in this case are displayed in Fig. 8.6b, which clearly show selective activations of the resonance modes of the skyrmion defect.

When the spin-wave modes of isolated skyrmions are activated in a system shown in Fig. 8.6c with a microwave electric field, their translational motion can be driven as shown in Fig. 8.6d. Figure 8.6e displays trajectories of the skyrmion translational motion when a microwave electric field with each resonance frequency is applied for a certain duration (Note that the length scale is different between the horizontal and vertical axes). Interestingly, the breathing mode turns out to drive the skyrmion most quickly although the intensity of this mode is not so large.

Another interesting aspect to be mentioned is the trajectory is straight and exactly parallel to the x axis (direction toward which the \mathbf{H}_{ex} field is tilted) when the counterclockwise rotation mode is excited. It is recognized that one of the most promising forms of the skyrmion-based magnetic memories is the skyrmion race track memory based on the skyrmion motion in magnetic nanowires driven by a spin-polarized electric current, which can be regarded as the race track memory with its ferromagnetic domains being replaced with magnetic skyrmions. However, one of the critical problems that hinders its realization is the skyrmion Hall effect. The current-driven skyrmions have not only a velocity component parallel to the electric current but also that perpendicular to it. Due to this effect, the skyrmion cannot avoid colliding to the horizontal edges of devices, which results in absorption and pinning of the skyrmions. In contrast to the current-driven case, we can achieve the translational motion of skyrmions exactly parallel to the nanowire and thus can avoid this kind of problem when we drive them by microwave irradiation under a tilted \mathbf{H}_{ext} field. For the breathing mode and the clockwise rotation mode, the skyrmion moves in a direction slanted from the tilting direction of the \mathbf{H}_{ex} field. Even in these cases, we can achieve the skyrmion motion exactly parallel to the nanowire by tuning the tilting direction of \mathbf{H}_{ex} . It is always possible to realize the straight and parallel skyrmion motion in a nanowire without collision to the edges in this way because the \mathbf{H}_{ex} field can be oriented in an arbitrary direction in contrast to an electric current flowing always along the nanowire.

8.6 Electrically Driven Spin Torque and Dynamical Dzyaloshinskii-Moriya Interaction

In the above section, we argued that the application of microwave electric field can drives translational motion of isolated skyrmions embedded in a ferromagnetic background of magnetic bilayer system through inducing the temporal variation of the interfacial Dzyaloshinskii-Moriya interaction. In this section, we discuss a theoretical formulation of this electrically induced time-dependent Dzyaloshinskii-Moriya interaction [35]. From a theoretical perspective, we demonstrate that the spin torques can be exerted into magnetic bilayer systems via the Rashba spin-orbit interaction by application of an AC electric voltage. The exerted spin torques turn out to resemble the well-known electric-current-induced torques, i.e., the spin-transfer torque and the nonadiabatic torque, providing similar controllability of magnetism with microwave electric fields. The spin torques also turn out to work as an interfacial Dzyaloshinskii-Moriya interaction, which contains both steady and oscillating components and enables us to create and activate noncollinear magnetism like magnetic skyrmions by application of a microwave electric field.

In the magnetic bilayer system with broken spatial inversion symmetry, the Rashba spin-orbit interaction becomes active. This interaction works as an effective magnetic field acting on the conduction-electron spins, through mediating mutual coupling between spins and orbital momenta of the electrons [38, 39]. Importantly, strength and direction of the effective magnetic field are determined by the momentum of the electron. Therefore, the Rashba spin-orbit interaction can induce nontrivial spin torques acting on the magnetizations through controlling the spin polarizations of the conduction electrons which couple to the magnetizations via the exchange interaction. The strength of the Rashba spin-orbit interaction can be tuned by application of a gate electric voltage normal to the interfacial plane [40], through modulating the extent of the spatial inversion asymmetry. This suggests that an AC gate voltage produces nontrivial Rashba-mediated dynamical spin torques.

We consider a magnetic bilayer system with a ferromagnet/heavy-metal interface (Fig. 8.7), which is fabricated on an insulating substrate. The insulating substrate prevents the electric-current flow and thus enhances the effects of gate electric voltage acting on the ferromagnet/heavy-metal interface. The Hamiltonian for this system has four terms as

$$H = H_K + H_R + H_{\text{ex}} + H_{\text{imp}} \quad (8.13)$$

with

$$H_K = \frac{1}{2m_e} \int d^2r |\mathbf{p}\psi(\mathbf{r}, t)|^2 - E_F \int d^2r \psi^\dagger(\mathbf{r}, t)\psi(\mathbf{r}, t), \quad (8.14)$$

$$H_R = -\frac{\alpha_R(t)}{\hbar} \int d^2r \psi^\dagger(\mathbf{r}, t)(\mathbf{p} \times \boldsymbol{\sigma})_z \psi(\mathbf{r}, t), \quad (8.15)$$

$$H_{\text{ex}} = J_{\text{ex}} \int d^2r \mathbf{m}(\mathbf{r}) \cdot \psi^\dagger(\mathbf{r}, t)\boldsymbol{\sigma}\psi(\mathbf{r}, t), \quad (8.16)$$

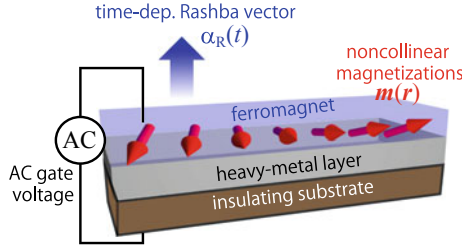


Fig. 8.7 Schematic illustration of a magnetic bilayer system in which local magnetizations $\mathbf{m}(\mathbf{r})$ couple to a conduction-electron system with the time-dependent Rashba spin-orbit interaction. The strength of the Rashba interaction $\alpha_R(t)$ is temporally varying under application of an AC gate electric voltage. The insulating substrate prevents electric-current flows to enhance the effects of electric voltage acting on the interface hosting the Rashba spin-orbit interaction (Reproduced from [35].)

$$H_{\text{imp}} = \int d^2r v_{\text{imp}}(\mathbf{r}) \psi^\dagger(\mathbf{r}, t) \psi(\mathbf{r}, t), \quad (8.17)$$

where m_e and \mathbf{p} denote, respectively, the mass and momentum of a conduction electron, E_F the Fermi energy, $\boldsymbol{\sigma}$ the Pauli matrices, and ψ^\dagger (ψ) the creation (annihilation) operator of a conduction electron. The term H_K represents the kinetic energies of the conduction electrons, while the term H_R describes the time-varying Rashba spin-orbit interaction where $\alpha_R(t)$ is the time-dependent coupling coefficient. The term H_{ex} represents the exchange interaction between the conduction-electron spins and the local magnetization where J_{ex} and \mathbf{m} are the coupling constant and the normalized local magnetization vector, respectively. The term H_{imp} depicts the scattering potentials from spatially distributed nonmagnetic impurities, which determine the relaxation time τ of the conduction electrons.

The impurity potential is given by,

$$v_{\text{imp}}(\mathbf{r}) = u_{\text{imp}} \sum_i \delta(\mathbf{r} - \mathbf{r}_i) \quad (8.18)$$

where u_{imp} is the strength of the impurity scattering, \mathbf{r}_i denotes positions of the impurities, and $\delta(\mathbf{r})$ is the Dirac delta function. Taking averages over the impurity positions as

$$\overline{v_{\text{imp}}(\mathbf{r})} = 0, \quad \overline{v_{\text{imp}}(\mathbf{r})v_{\text{imp}}(\mathbf{r}')} = n_{\text{imp}}u_{\text{imp}}^2\delta(\mathbf{r} - \mathbf{r}'), \quad (8.19)$$

the relaxation time of the conduction electrons is given by

$$\tau = \hbar/2\pi v_e n_{\text{imp}} u_{\text{imp}}^2 \quad (8.20)$$

in the first Born approximation. Here, n_{imp} denotes the concentration of impurities and $v_e = m_e/2\pi\hbar^2$ is the density of state.

The spin torque induced by the conduction-electron spins via the exchange interaction is defined as

$$\mathbf{T} = \frac{J_{\text{ex}} a^2}{\hbar} \mathbf{m} \times \mathbf{s}, \quad (8.21)$$

where a is the lattice constant, $\mathbf{s} = \langle \psi^\dagger \boldsymbol{\sigma} \psi \rangle$ is the conduction-electron spin density, and the brackets denote the quantum expectation value. The analytical formula of the spin torque is given in the form,

$$\begin{aligned} \mathbf{T} &= \mathbf{T}_1 + \mathbf{T}_2 + \mathbf{T}_3 \\ &= -\frac{a}{\hbar} D_1 (\mathbf{m} \times \nabla)_z \mathbf{m} + \frac{a}{\hbar} D_2 (\mathbf{m} \times \nabla)_z \mathbf{m} \\ &\quad - \frac{a}{\hbar} \beta_{\text{R}} D_2 \mathbf{m} \times \left[(\mathbf{m} \times \nabla)_z \mathbf{m} \right], \end{aligned} \quad (8.22)$$

where

$$D_1(t) = \frac{\hbar v_{\text{e}} a}{2\pi \tau} \left[\frac{E_{\text{F}}}{J_{\text{ex}}} \ln \left(\frac{E_{\text{F}} + J_{\text{ex}}}{E_{\text{F}} - J_{\text{ex}}} \right) - 2 \right] \alpha_{\text{R}}(t), \quad (8.23)$$

$$D_2(t) = v_{\text{e}} a E_{\text{F}} \tau \frac{J_{\text{ex}}^2 (J_{\text{ex}}^2 - \eta^2)}{(J_{\text{ex}}^2 + \eta^2)^2} \frac{d\alpha_{\text{R}}(t)}{dt}, \quad (8.24)$$

$$\beta_{\text{R}} = \frac{2J_{\text{ex}}\eta}{J_{\text{ex}}^2 - \eta^2}, \quad (8.25)$$

with $\eta = \hbar/2\tau$.

The above formula is derived from perturbation calculations based on some assumptions summarized below:

- Metallic bilayer systems with $J_{\text{ex}} < E_{\text{F}}$,
- Slowly varying magnetizations with $q \ll k_{\text{F}}$,
- Weak magnitudes α_{R} with $\alpha_{\text{R}} k_{\text{F}} \ll E_{\text{F}}$,
- Low frequencies Ω for α_{R} with $\hbar\Omega \ll E_{\text{F}}$,

where q is the wavenumber of local magnetization and k_{F} is the Fermi wavenumber. The coefficients $D_1(t)$, $D_2(t)$, and β_{R} are well defined when the relaxation time is sufficiently long to satisfy the conditions $E_{\text{F}} \gg \hbar/\tau$, $J_{\text{e}} \gg \hbar/\tau$ and $E_{\text{F}} - J_{\text{ex}} \gg \hbar/\tau$. Note that D_1 vanishes in the clean limit with $\tau \rightarrow \infty$ for the present quasi-two-dimensional metallic system with $J_{\text{ex}} < E_{\text{F}}$, whereas it is known to survive in the three-dimensional systems or in the half-metallic systems with $J_{\text{ex}} > E_{\text{F}}$ even in the clean limit. For details of the derivation, see [35].

The first two contributions in (8.22), $\mathbf{T}_1 + \mathbf{T}_2$, describe an effective Dzyaloshinskii-Moriya interaction, which is given in the continuum form as

$$\mathcal{H}_{\text{DMI}} = \frac{D_1 - D_2}{a} \epsilon_{\alpha\beta z} \int d^2 r (\mathbf{m} \times \nabla_{\alpha} \mathbf{m})^{\beta}. \quad (8.26)$$

Table 8.2 Typical material parameters for magnetic bilayer systems

	Metallic systems	Semiconducting systems
Lattice constant a	5 Å	5 Å
Fermi energy E_F	4 eV	10 meV
Fermi wavenumber k_F	1 Å ⁻¹	0.01 Å ⁻¹
Exchange int. J_{ex}/E_F	0.25	0.5
Relaxation time τ	10 ⁻¹⁴ s	10 ⁻¹² s
Rashba parameter 1: α_0	2 eV·Å	0.07 eV·Å
Rashba parameter 2: $\alpha_{\text{ext}}/\alpha_0$	0.1	0.1
Frequency $\Omega/2\pi$	1 GHz	1 GHz

(Note that $\mathbf{m} \times (a^2/\hbar)\delta\mathcal{H}_{\text{DMI}}/\delta\mathbf{m}$ leads to $\mathbf{T}_1 + \mathbf{T}_2$). The contribution D_1 , which is proportional to α_R , appears even with a steady Rashba spin-orbit interaction. In contrast, the contribution D_2 , which is proportional to $\partial_t\alpha_R$, appears only in the presence of a time-dependent Rashba spin-orbit interaction. This interfacial Dzyaloshinskii-Moriya interaction is expected to be tuned by applying an electric gate voltage. More interestingly, application of an AC voltage is expected to induce an oscillating component of the Dzyaloshinskii-Moriya interaction. The Rashba parameter $\alpha_R(t)$ in the driven Rashba electron system is composed of both steady and time-dependent components as $\alpha_R(t) = \alpha_0 + \alpha_{\text{ext}}(t)$ with $\alpha_{\text{ext}}(t) = \alpha_{\text{ext}} \sin(\Omega t)$. Using typical material parameters summarized in Table 8.2 [40–42], the strength of this Rashba-induced Dzyaloshinskii-Moriya interaction is roughly estimated as $D_1 \sim 0.1$ meV and $D_2 \sim 5 \times 10^{-3}$ meV for metallic bilayer systems, while $D_1 \sim 6 \times 10^{-6}$ meV and $D_2 \sim 2 \times 10^{-6}$ meV for semiconducting bilayer systems. The strength of the Rashba-induced Dzyaloshinskii-Moriya interaction is relatively strong in metallic bilayer systems, whereas it is rather weak in the semiconducting bilayer systems.

It should be mentioned that the magnitude of D_2 being proportional to $\partial_t\alpha_{\text{ext}}(t)$ can be tuned by varying the amplitude and frequency of the AC gate voltage, although it is usually small as compared to the magnitude of D_1 . The ratio D_2/D_1 is approximately given by $\Omega\varepsilon_F\tau^2/2\pi\hbar$, which takes $\sim 10^{-4}$ (10^{-2}) for metallic (semiconducting) bilayer systems when a typical frequency of $\Omega = 1$ GHz is assumed. The ratio D_2/D_1 tends to be larger for the semiconducting system, whereas the absolute value of D_2 tends to be larger for the metallic system. An appropriate system should be chosen depending on the purpose.

The last two terms in (8.22), both of which are proportional to D_2 , can be rewritten as

$$\mathbf{T}_2 + \mathbf{T}_3 \propto (\mathbf{j}_s \cdot \nabla)\mathbf{m} - \beta_R \mathbf{m} \times (\mathbf{j}_s \cdot \nabla)\mathbf{m}. \quad (8.27)$$

where

$$\mathbf{j}_s \equiv (e/\hbar a)D_2\mathbf{z} \times \mathbf{m}. \quad (8.28)$$

When the time-dependent Rashba spin-orbit interaction $\alpha_R(t)$ is induced by the AC gate voltage, the vector quantity $\mathbf{j}_s \propto \partial_t \alpha_R(t) \mathbf{z} \times \mathbf{m}$ gives rise to AC spin torques. In the clean limit with a long relaxation time ($\hbar/J_{\text{ex}}\tau \ll 1$), the coefficient β_R in the second term is reduced to $\hbar/J_{\text{ex}}\tau$. Interestingly, the vector quantity \mathbf{j}_s defined here can be regarded as a fictitious spin current because the above expressions of \mathbf{T}_2 and \mathbf{T}_3 have equivalent forms with those of the spin-transfer torque and the nonadiabatic torque in the presence of the real spin current \mathbf{j}_s , respectively. It should be noted, however, the present relaxation time τ corresponds to a different time scale. Specifically, the relaxation time is governed by the coherence of the conduction-electron momenta in the present case, while in the current-induced case, it is governed by that of the conduction-electron spins.

Assuming the material parameters for the metallic bilayer systems in Table 8.2, the values of $j_s = (e/\hbar a)D_2$ and β_R are evaluated as ~ 2 A/m and ~ 0.07 , respectively. These values are large enough to induce the magnetization dynamics. Numerical simulations in [35] indeed demonstrated that not only a skyrmion crystal with hexagonally packed magnetic skyrmions but also isolated skyrmions embedded in a ferromagnetic background can be excited resonantly through temporal variation of the Dzyaloshinskii-Moriya interaction achieved by application of a microwave electric voltage. This technique provides a means to drive magnetic skyrmions electrically with a low energy consumption. Recently, a lot of ferromagnet/heavy-metal bilayer systems hosting magnetic skyrmions have been reported. The above theoretical proposals are anticipated to be realized by future experiments on these magnetic bilayer systems.

8.7 Microwave-Induced DC Spin-Motive Force

We next discuss a proposed method to generate DC electric voltages by exploiting the spin-wave excitations of magnetic skyrmions under a tilted \mathbf{H}_{ext} field [31]. It is well known that injection of spin-polarized electric currents can drive non-collinear skyrmion textures in metallic magnets via the spin-transfer torque mechanism, whereas the noncollinear skyrmion magnetizations inversely affect transport properties of conduction electrons as exemplified by the topological Hall effect. The spin-driven electromotive force (i.e., an emergent electric field induced by magnetization dynamics) is another important example of the latter kinds of phenomena [43, 44]. It was proposed theoretically that spatially modulated magnetic textures such as magnetic skyrmions, magnetic helices and ferromagnetic domain walls produce effective vector potential acting on the conduction electrons via exchange coupling with the conduction-electron spins, which is called non-Abelian gauge field. When these magnetic textures are temporally varied by an applied time-periodic field such as microwave electromagnetic fields, this effective vector potential also changes temporally. This temporal variation of the vector potential gives rise to an effective electric field which acts on the conduction electrons. The electric motive force due to this effective electric field is referred to as the spin-motive force, which is one of

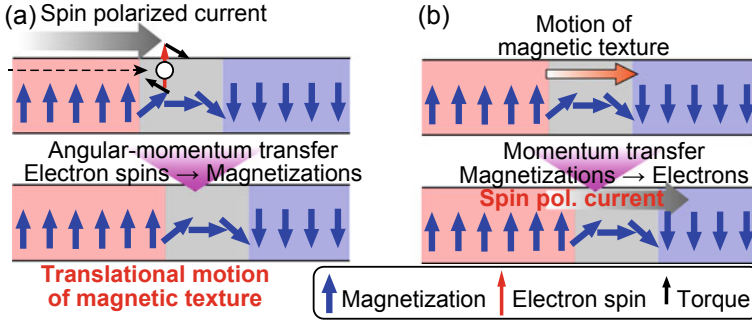


Fig. 8.8 Relationship between the spin-transfer torque mechanism and the spin-motive force. **a** Schematic illustrations of the spin-transfer torque mechanism. Translational motion of a magnetic texture is driven by the angular-momentum transfer from conduction-electron spins of injected spin-polarized currents to the noncollinear magnetizations. **b** Schematic illustrations of the spin-motive force. Effective electromotive force acting on the conduction electrons is induced by the momentum transfer from driven noncollinear magnetic texture to the conduction electrons via exchange coupling, resulting in the generation of electric currents (Reproduced from [31].)

the important subjects of the recent spintronics research. This phenomenon can be interpreted as the inverse effect of the spin-transfer torque mechanism (see Fig. 8.8).

An expression of this spin-induced effective electric field is given by,

$$E_{\mu}(t) = \frac{\hbar}{2e} \mathbf{m} \cdot (\partial_{\mu} \mathbf{m} \times \partial_t \mathbf{m}) \quad (\mu = x, y, z), \quad (8.29)$$

where $\mathbf{m}(\mathbf{r}, t)$ is the normalized classical magnetization vector. This formula explicitly indicates that both temporal and spatial variations of magnetizations are required to generate the spin-motive force. Several experimental reports have discussed the generation and observation of the spin-motive force in ferromagnetic domain walls and magnetic vortices activated by microwave fields [45, 46].

There has been a theoretical proposal that the microwave activation of skyrmion crystal under a perpendicular \mathbf{H}_{ex} field gives rise to an enhanced spin-motive force [47, 48]. However, the spin-motive force available in this way is a pure AC voltage with an average of zero. In fact, there have been several theoretical proposals and experimental demonstrations of the generation of the AC spin-motive force. However, a method to generate a stationary DC spin-motive force has long been missing. One possible way to obtain a DC voltage is to use an AC-DC transducer to convert the AC voltage to a DC voltage. But it is difficult to fabricate such a precise device in nanometric systems. Moreover, significant reduction of the voltage cannot be avoided in the conversion process, which can be a critical problem because the spin voltage is originally very tiny. Therefore, it is highly desired to establish a simple technique to generate a DC spin voltage for spintronics applications.

To solve this problem, it was recently proposed theoretically that an oscillating spin voltage with a large DC component can be generated by exciting the microwave-

active spin-wave modes of skyrmion crystal on a quasi-two-dimensional thin-plate magnet under a tilted \mathbf{H}_{ex} field in [31]. In this study, micromagnetic simulations based on the Landau–Lifshitz–Gilbert equation were performed to trace the magnetization dynamics of a skyrmion crystal activated by a microwave magnetic field \mathbf{H}^ω . Using the simulated data of the magnetization dynamics, the spatiotemporal profiles of the spin-motive force $\mathbf{E}(\mathbf{r}, t)$ were numerically calculated. For the numerical calculations, it is convenient to rewrite (8.29) in discretized form as

$$E_{\mu,i}(t) = \frac{\hbar}{2e} \mathbf{m}_i(t) \cdot \left[\frac{\mathbf{m}_{i+\hat{\mu}}(t) - \mathbf{m}_{i-\hat{\mu}}(t)}{2a} \times \frac{\mathbf{m}_i(t + \Delta t) - \mathbf{m}_i(t - \Delta t)}{2\Delta t} \right], \quad (8.30)$$

where $\mu = x, y$ and $a(=5 \text{ \AA})$ is the lattice constant. Time profiles of the spin voltage were calculated by numerically solving the Poisson equation using the spatial distribution data of the spin-motive force $\mathbf{E}(\mathbf{r}, t)$ at each moment t .

The spin-motive force that contains a large DC component can indeed be generated by activation of the spin-wave modes of magnetic skyrmions under a tilted \mathbf{H}_{ext} field. Figure 8.9a–d show time profiles of the spin-motive force simulated for a $50 \text{ nm} \times 50 \text{ nm}$ squared system which contains a skyrmion crystal composed of twelve skyrmions. When the \mathbf{H}_{ex} field is perpendicular, the generated spin-motive force is of pure AC for the counterclockwise rotation mode (Fig. 8.9a) or constantly zero for the breathing mode (Fig. 8.9b). On the contrary, a spin-motive force with a large DC component of $0.5\text{--}1 \text{ \mu V}$ is generated when the \mathbf{H}_{ex} field is tilted by $\theta = 30^\circ$ (Fig. 8.9c, d).

The simulated time profiles of spin voltages turn out to be well fitted by an approximate formula of the forced oscillation with a damping.

$$V_\mu = V_\mu^{\text{DC}} + V_\mu^{\text{AC}}(1 - e^{-t/\tau}) \sin \omega t, \quad (8.31)$$

with $\mu = x, y$. Here V_μ^{DC} , V_μ^{AC} , $\omega(= 2\pi f)$, and τ are the DC component, the AC amplitude, the angular frequency, and the decay rate of the induced temporally oscillating spin voltage, respectively. Fig. 8.9e–f show the microwave-frequency dependence of the DC component V_μ^{DC} ($\mu = x, y$) for different microwave polarizations, which are evaluated by the fitting. Specifically, Fig. 8.9e shows V_x^{DC} for $\mathbf{H}^\omega \parallel \mathbf{x}$, y, Fig. 8.9f shows V_y^{DC} for $\mathbf{H}^\omega \parallel \mathbf{x}$, y, Fig. 8.9g shows V_x^{DC} for $\mathbf{H}^\omega \parallel \mathbf{z}$, and Fig. 8.9h shows V_y^{DC} for $\mathbf{H}^\omega \parallel \mathbf{z}$. The results show that the DC component is enhanced significantly when the frequency of the microwave is tuned to an eigenfrequency of the spin-wave modes, which converts the microwave power to a DC voltage with high efficiency. The results also show that the sign of the DC voltage depends on the excited spin-wave mode and the microwave polarization, which indicates that the sign of the voltage can be switched by tuning the microwave frequency or the microwave polarization. Note that a large DC voltage is obtained for the counterclockwise rotation mode activated by $\mathbf{H}^\omega \parallel \mathbf{x}$, y and for the breathing mode activated by $\mathbf{H}^\omega \parallel \mathbf{z}$,

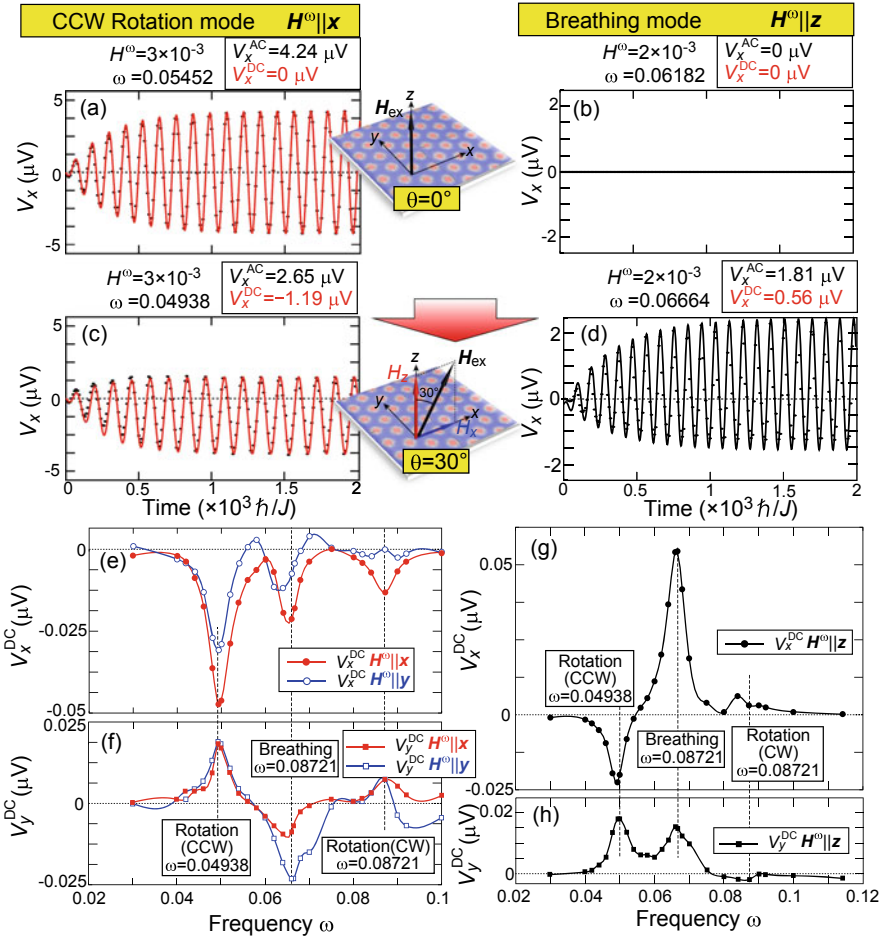


Fig. 8.9 **a, b** Calculated time profiles of spin voltages induced by **a** the counterclockwise (CCW) rotation mode activated by a microwave field $H^\omega \parallel x$ and **b** the breathing mode activated by a microwave field $H^\omega \parallel z$ of a skyrmion crystal confined in a quasi-two-dimensional magnet under a perpendicular H_{ex} field with $\theta = 0^\circ$. **c, d** Those under a tilted H_{ex} field with $\theta = 30^\circ$. The amplitude H^ω and frequency ω of microwave are presented where $\omega (=2\pi f)$ is fixed at the eigenfrequency of the spin-wave mode. The DC component V_x^{DC} evaluated by fitting the simulated time profiles are shown as well. **e-h** Calculated microwave-frequency dependence of the DC component V_μ^{DC} ($\mu = x, y$) of the spin voltage under a tilted H_{ex} field with $\theta = 30^\circ$, i.e., **e** V_x^{DC} for $H^\omega \parallel x, y$, **f** V_y^{DC} for $H^\omega \parallel x, y$, **g** V_x^{DC} for $H^\omega \parallel z$, **h** V_y^{DC} for $H^\omega \parallel z$. The microwave amplitude is fixed at $H^\omega = 0.6 \times 10^{-3}$ for **e-h**. The parameters are fixed at $J = 1$, $D = 0.27$, $H_z = 0.036$, and $\alpha = 0.04$, whereas the system of $N = 96 \times 111$ sites with a skyrmion crystal composed of twelve magnetic skyrmions is used for all the simulations (Reproduced from [31].)

which indicates that these sets of microwave polarization and the spin-wave mode are suitable for efficient conversion of microwaves to a DC electric voltage.

It should be also noted that an advantage of using a skyrmion crystal is that the arrays of numerous magnetic skyrmions in a skyrmion crystal behaves as batteries connected in series, which give a large electric voltage as a sum of each contribution. We expect several orders of magnitude larger electric voltage by using a larger-sized device, which offers a promising technique of an efficient conversion of microwaves to DC electric voltages.

8.8 Concluding Remarks

To summarize this chapter, we have discussed several microwave-related phenomena that magnetic skyrmions confined in a quasi-two-dimensional magnetic specimen are expected to show under a tilted external magnetic field by particularly taking the microwave-driven translational motion and the microwave-induced DC spin-motive forces as topics. The researches on the dynamical phenomena and device functions of magnetic skyrmions are now extended over a wide area. The researches on magnetic skyrmions which bring technical applications into a scope can be classified roughly into two categories. One category of the researches aims for application to magnetic memories and storage devices and seek the elementary techniques to write, erase, read, and drive magnetic skyrmions in controlled ways [3, 49]. Another category of the researches focuses on the microwave-device functions of magnetic skyrmions based on their peculiar spin-wave modes such as microwave generation, microwave detection, microwave diode, and magnonic-crystal devices [4, 6, 7]. In addition, magnetic skyrmions nowadays became to attract novel research interest as promising building blocks of logic-gate devices [50] and brain-inspired computing devices such as reservoir computing [51–53] and neuromorphic computing [54, 55]. It is yet to be clarified what kinds of technical applications can be expected for the phenomena discussed in this chapter. However, we naively anticipate that the magnetic skyrmions under a tilted \mathbf{H}_{ext} field are still hiding a lot of intriguing phenomena, useful device functions, and novel physics, which might be clarified in future studies.

References

1. S. Seki, M. Mochizuki, *Skyrmions in Magnetic Materials* (Springer, Berlin, 2015)
2. N. Nagaosa, Y. Tokura, *Nat. Nanotechnol.* **8**, 899 (2013)
3. A. Fert et al., *Nat. Nanotechnol.* **8**, 152 (2013)
4. G. Finocchio et al., *J. Phys. D: Appl. Phys.* **49**, 423001 (2016)
5. K. Everschor-Sitte et al., *J. Appl. Phys.* **124**, 240901 (2018)
6. M. Garst et al., *J. Phys. D: Appl. Phys.* **50**, 293002 (2017)
7. M. Mochizuki, S. Seki, *J. Phys.: Condens. Matter* **27**, 503001 (2015)
8. T.H.R. Skyrme, *Proc. R. Soc. A* **260**, 127 (1961)

9. T.H.R. Skyrme, Nucl. Phys. **31**, 556 (1962)
10. A.N. Bogdanov, D.A. Yablonskii, Sov. Phys. JETP **68**, 101 (1989)
11. A. Bogdanov, A. Hubert, J. Magn. Magn. Mat. **138**, 255 (1994)
12. S. Mühlbauer et al., Science **323**, 915 (2009)
13. X.Z. Yu et al., Nature **465**, 901 (2010)
14. X.Z. Yu et al., Nat. Mater. **10**, 106 (2011)
15. S. Seki et al., Science **336**, 198 (2012)
16. Y. Tokunaga et al., Nat. Commun. **6**, 7638 (2015)
17. I. Kezsmarki et al., Nat. Mater. **14**, 1116 (2012)
18. S. Bordács et al., Sci. Rep. **7**, 7584 (2017)
19. Y. Fujima et al., Phys. Rev. B **95**, 180410(R) (2017)
20. A. Nayak et al., Nature **548**, 561 (2017)
21. T. Kurumaji et al., Phys. Rev. Lett. **119**, 237201 (2017)
22. C. Moreau-Luchaire et al., Nat. Nanotechnol. **11**, 444 (2016)
23. G. Chen et al., Appl. Phys. Lett. **106**, 242404 (2015)
24. O. Boulle et al., Nat. Nanotechnol. **11**, 449 (2016)
25. I.E. Dzyaloshinskii, Sov. Phys. JETP **5**, 1259 (1957)
26. T. Moriya, Phys. Rev. **120**, 91 (1960)
27. M. Mochizuki, Phys. Rev. Lett. **108**, 017601 (2012)
28. W. Wang et al., Phys. Rev. B **92**, 020403(R) (2015)
29. M. Ikka et al., Phys. Rev. B **98**, 184428 (2018)
30. A. Takeuchi, M. Mochizuki, Appl. Phys. Lett. **113**, 072404 (2018)
31. T. Koide et al., Phys. Rev. B **100**, 014408 (2019)
32. P. Bak, M.H. Jensen, J. Phys. C **13**, L881 (1980)
33. S.D. Yi et al., Phys. Rev. B **80**, 054416 (2009)
34. A. Tonomura et al., Nano Lett. **12**, 1673 (2012)
35. A. Takeuchi et al., Sci. Rep. **9**, 9528 (2019)
36. K. Nawaoka et al., Appl. Phys. Exp. **8**, 063004 (2015)
37. T. Srivastava et al., Nano Lett. **18**, 4871 (2018)
38. I.E. Rashba, Sov. Phys. Solid State **2**, 1109 (1960)
39. A. Manchon et al., Nat. Mater. **14**, 871 (2015)
40. J. Nitta et al., Phys. Rev. Lett. **78**, 1335 (1997)
41. C.R. Ast et al., Phys. Rev. Lett. **98**, 186807 (2007)
42. T. Nakagawa et al., Phys. Rev. B **75**, 155409 (2007)
43. G.E. Volovik, J. Phys. C **20**, L83 (1987)
44. S.E. Barnes, S. Maekawa, Phys. Rev. Lett. **98**, 246601 (2007)
45. S.A. Yang et al., Phys. Rev. Lett. **102**, 067201 (2009)
46. K. Tanabe et al., Nat. Commun. **3**, 845 (2012)
47. J. Ohe, Y. Shimada, Appl. Phys. Lett. **103**, 242403 (2013)
48. Y. Shimada, J.I. Ohe, Phys. Rev. B **91**, 174437 (2015)
49. W. Koshibae et al., Jpn. J. Appl. Phys. **54**, 053001 (2015)
50. X. Zhang et al., Sci. Rep. **5**, 9400 (2015)
51. D. Pinna et al., Phys. Rev. Appl. **9**, 064018 (2018)
52. D. Prychynenko et al., Phys. Rev. Appl. **9**, 014034 (2018)
53. G. Bourianoff et al., AIP Adv. **8**, 055602 (2018)
54. Z. He, D. Fan, [arXiv:1705.02995](https://arxiv.org/abs/1705.02995)
55. X. Chen et al., Nanoscale **10**, 6139 (2018)